



Universidad Autónoma  
de Madrid

**Biblos-e Archivo**  
Repositorio Institucional UAM

**Repositorio Institucional de la Universidad Autónoma de Madrid**

<https://repositorio.uam.es>

Esta es la **versión de autor** del artículo publicado en:  
This is an **author produced version** of a paper published in:

Advanced Healthcare Materials 10.10 (2021): 2002186

**DOI:** <https://doi.org/10.1002/adhm.202002186>

**Copyright:** © 2021 Wiley-VCH GmbH

El acceso a la versión del editor puede requerir la suscripción del recurso  
Access to the published version may require subscription

DOI: 10.1002/ ((please add manuscript number))

Article type: **Full Paper**

## **Molecular Imaging of infarcted heart by biofunctionalized Gold Nanoshells**

*Tamara Muñoz-Ortiz, Jie Hu, Dirk H. Ortgies, Shreya. Shrikhande, Paula Zamora-Pérez, Miriam Granado, Daniel González-Hedström, María de la Fuente-Fernández, Ángel Luis Villalón, Laura de Andrés-Delgado, Emma Martín Rodríguez, Río Aguilar, Fernando Alfonso, José García Solé, Pilar Rivera Gil, Fernando Rivero, and Daniel Jaque\*.*

T. Muñoz-Ortiz, Dr. D. H. Ortgies, Prof. J. García Solé, Prof. D. Jaque  
Fluorescence Imaging Group, Departamento de Física de Materiales, Universidad Autónoma de Madrid, C/Francisco Tomás y Valiente 7, 28049 Madrid, Spain.

E-Mail: daniel.jaque@uam.es

Dr. J. Hu

Xiamen Institute of Rare-earth Materials, Haixi Institutes, Chinese Academy of Sciences  
258 Duishanxiheng Road, Jimei District, 361024 Xiamen, Fujian, China.

Dr. D. H. Ortgies, Prof. E. Martín Rodríguez, Prof. D. Jaque

Instituto Ramón y Cajal de Investigación Sanitaria, Hospital Ramón y Cajal, Ctra. Colmenar km. 9.100, 28034 Madrid, Spain.

S. Shrikhande, P. Zamora-Pérez, Dr. Habil. P. Rivera Gil

Integrative Biomedical Materials and Nanomedicine Lab, Department of Experimental and Health Sciences, Pompeu Fabra University, Carrer Doctor Aiguader 88, 08003 Barcelona, Spain.

Prof. M. Granado, D. González-Hedström, M. de la Fuente-Fernández, Prof. A.L. Villalón  
Fluorescence Imaging Group, Departamento de Fisiología, Facultad de Medicina, Universidad Autónoma de Madrid, C/Arzobispo Morcillo s/n, 28029 Madrid, Spain.

Prof. Laura de Andrés-Delgado

Departamento de Anatomía, Histología y Neurociencia. Facultad de Medicina. Universidad Autónoma de Madrid. C/Arzobispo Morcillo s/n, 28029 Madrid, Spain.

Prof. Emma Martín Rodríguez

Fluorescence Imaging Group, Departamento de Física Aplicada, Universidad Autónoma de Madrid, C/Francisco Tomás y Valiente 7, 28049 Madrid, Spain.

M.D. R. Aguilar, M.Dr. F. Alfonso, M. Dr. F. Rivero

Cardiology Department, Hospital Universitario de la Princesa, Instituto Investigación Sanitaria Princesa (IIS-IP), CIBER-CV, Universidad Autónoma de Madrid, Calle Diego de León, 62, 28006 Madrid, Spain.

Keywords: Gold Nanoshells, Optical Coherence Tomography, Infarct, Surface functionalization.

## Abstract

The unique combination of physical and optical properties of silica (core)/gold (shell) nanoparticles (gold nanoshells) makes them especially suitable for biomedicine. Gold nanoshells have been used from high-resolution *in vivo* imaging to *in vivo* photothermal tumor treatment. Furthermore, their large scattering cross section in the second biological window (1000-1700 nm) make them also especially adequate for molecular optical coherence tomography (OCT). In this work, we demonstrate how, after suitable functionalization, gold nanoshells in combination with clinical OCT systems are capable of imaging damage in the myocardium following an infarct. Since both inflammation and apoptosis are two of the main mechanisms underlying myocardial damage after ischemia, such damage imaging is achieved by endowing gold nanoshells with selective affinity for the inflammatory marker Intercellular Adhesion Molecule 1 (ICAM-1), and the apoptotic marker phosphatidylserine (PS). The results here presented constitute a first step towards a fast, safe, and accurate diagnosis of damaged tissue within infarcted hearts at the molecular level by means of the highly sensitive OCT interferometric technique.

## 1. Introduction.

Medical imaging of damaged myocardial tissues constitutes a valuable prognostic tool for patients with ischemic heart disease. Localization of myocardial damage is typically achieved by using either nuclear or magnetic resonance imaging (MRI) contrast agents. Some of them, such as those containing gadolinium as MRI contrast agent, are contraindicated for patients with renal impairment, whereas others, such as gamma ray-emitting tracers, imply the use of ionizing radiation that could lead to the appearance of undesirable collateral effects.<sup>[1]</sup> In order to avoid those limitations new biocompatible contrast agents<sup>[2]</sup> are being developed for myocardium imaging with alternative technologies.<sup>[3]</sup> Among them, optical nanoparticles (ONPs) capable of absorbing, scattering, or emitting infrared light have emerged as a reliable alternative.<sup>[4]</sup> The good penetration of infrared light into tissues allows for high resolution depth imaging.<sup>[5]</sup> In addition, the non-ionizing character of infrared light minimizes the collateral effects caused during imaging experiments. Of special relevance are gold nanoparticles (AuNPs) due to their unique combination of properties.<sup>[6]</sup> These include excellent long-term stability, fast and inexpensive synthesis, and facile surface biofunctionalization.<sup>[7]</sup> Reports of *in vivo* toxicity and biodistribution of large gold nanostructures (as the ones presented herein) in mice propose that nanoparticles between 60 and 200 nm are mainly accumulated in the liver and the spleen.<sup>[8]</sup> Studies carried out for long times after the injections of AuNPs solutions conclude that gold is cleared from the liver within the first month, but further research into clearance by the spleen is necessary since literature does not provide a unique conclusion.<sup>[8d, 8e]</sup> Even if there is a clear accumulation in both organs, no histological or biochemical changes have been reported up to date. A simple *in vitro* toxicity test of the commercial AuNPs used along this work is provided elsewhere<sup>[9]</sup>, showing that no *in vitro* toxicity of the AuNPs is noticed.

The morphology-dependent plasmon resonance of AuNPs leads to an enhanced optical response at selected wavelengths that has been extensively employed in preclinical studies.<sup>[10]</sup>

AuNPs have been used for cardiovascular studies enabling, for instance, imaging of brain vasculature, thrombus detection by photoacoustic imaging, angiogenesis monitoring, drug delivery to myocardium tissues, enhancement of myocardial regeneration and retinal vessels visualization.<sup>[11]</sup> Recently, it was demonstrated how an appropriate biofunctionalization of AuNPs allows imaging of myocardial scarring by using them as contrast agents in computed tomography, *i.e.* not by the non-invasive optical methods.<sup>[12]</sup>

Optical Coherence Tomography (OCT) is a pure optical technique capable of in-depth tissue visualization that is based on the analysis of back-scattered infrared radiation by tissues. Originally used for ophthalmology,<sup>[13]</sup> OCT is now being used in hemodynamic and interventional cardiology units.<sup>[14]</sup> Indeed, clinical equipment already exists combining OCT optical systems with catheters for intracoronary imaging. Due to their large scattering cross sections, AuNPs of different morphologies were previously proposed as efficient intravascular OCT contrast agents. For instance, gold nanoroses have been used as contrast agents for OCT imaging of atheroma plaques in rabbit aorta.<sup>[15]</sup> Among the great variety of AuNPs, gold nanoshells (GNSs) demonstrated to be the best contrast agents among those commercially available.<sup>[16]</sup> Nevertheless, a systematic comparison of the scattering properties of differently sized and shaped AuNPs (commercially and not commercially available) can be seen in the Supporting Information section (**Figure S1**). Besides, GNSs' optical properties can be easily tuned in the synthesis process.<sup>[7e]</sup> Furthermore, it has also been postulated that spherical nanoparticles, as GNSs, could be especially indicated for *in vivo* molecular imaging. Indeed, when intravenously administered, spherical NPs interact more efficiently with cells than other geometries<sup>[17]</sup> such as elongated NPs, because the latter are extended by the flow.<sup>[18]</sup> In addition, GNSs combine their large scattering cross section at near infrared wavelengths of interest with high photothermal conversion efficiency, making possible their use as contrast agents not only

in conventional OCT<sup>[19]</sup> but also, in photothermal OCT. <sup>[19a]</sup> Finally, a very important aspect; the possible clinical application of GNSs as therapeutic agents has recently been demonstrated, supporting the feasibility of the near future application of GNSs in the clinics.<sup>[20]</sup> Despite all these advantages and promising results, the use of GNSs for imaging of the infarcted myocardium has not been explored yet.

Infarct imaging at molecular level with GNSs requires their functionalization with suitable ligands for specific targets overexpressed in damaged myocardial tissues. Ischemia induces complex changes in cardiomyocytes that result in the upregulation and overexpression of different targets. Thus, different approaches do exist, among all of them inflammation and damage targeting result of special relevance:

- i) Ischemia-induced inflammation can be imaged with nanoparticles functionalized with peptides or antibodies dedicated to targeting the intercellular adhesion molecule (ICAM-1). ICAM-1 plays an important role in a number of cellular events, including adhesion of leukocytes to the endothelium followed by their emigration into sites of inflammation.<sup>[21]</sup> ICAM-1 is expressed on the surface of a wide variety of cell types.<sup>[22]</sup> In cardiomyocytes, mRNA and protein levels of this adhesion molecule are up-regulated after acute ischemia,<sup>[22]</sup> both in animals<sup>[23]</sup> and in humans.<sup>[24]</sup> This up-regulation is mediated by an increase in pro-inflammatory cytokines such as IL-6,<sup>[25]</sup> TNF- $\alpha$ <sup>[26]</sup> or IL-1 $\beta$ .<sup>[23c]</sup> It was reported that ICAM-1 overexpression mediates, at least in part, the ischemia-induced damage of myocardial tissue, and that inhibition of its expression in the heart dramatically reduces both the infiltration of immune cells and the infarct size.<sup>[22]</sup>
- ii) Targeting the ischemia-induced apoptosis of cardiomyocytes by anti-phosphatidylserine (anti-PS) functionalized probes constitutes an alternative route for imaging the infarcted heart. Apoptosis takes place during reperfusion and is associated with loss of membrane phospholipid asymmetry, which is one of the main

mechanisms that allows macrophages to recognize cells that are undergoing apoptosis.<sup>[27]</sup> The remodelling of the cell membrane in apoptotic cells is associated with a reduction of amino phospholipid translocase, resulting in translocation of phospholipids such as PS and phosphatidylethanolamine into the outer leaflet of the cell membrane.<sup>[28]</sup> This translocation makes possible the recognition of PS by macrophages in order to rapidly eliminate the apoptotic cells.<sup>[29]</sup>

The aim of this work is to take advantage of the large infrared scattering cross section of GNSs combined with state-of-the art intravascular OCT systems in order to visualize the damaged myocardium after an ischemic event. Selective accumulation of GNSs at damaged myocardial sites was achieved by proper surface decoration with both anti-PS or anti-ICAM-1 ligands, providing them with high affinity to cardiomyocytes subjected to both inflammation and apoptosis, respectively. *Ex vivo* images of infarcted hearts perfused with these functionalized GNSs were obtained. The differences between the OCT images of the healthy and infarcted myocardium were critically analysed and the potential of GNSs as molecular contrast agents for heart studies has been evaluated.

## 2. Results and Discussion.

In this work we used commercial GNSs provided by Nanocomposix. **Figure 1(a)** shows a typical TEM picture of the GNSs, revealing their homogeneous size distribution as well as their spherical shape. They consist of a 200 nm diameter silica core surrounded by a 20 nm thick gold shell (see schematic drawing in the inset of **Figure 1(b)**). These GNSs show a broad plasmonic extinction band spanning from the visible up to the infrared that leads to a high extinction coefficient at the operating wavelength of cardiovascular OCT systems (1320 nm as indicated in **Figure 1(b)**). **Figure 1(c)** schematizes our approach for the detection of damaged cardiomyocytes. It implies, as stated previously, the use of anti-PS or anti-ICAM-1

functionalized GNSs to target apoptosis and inflammation, respectively. A detailed description of the functionalization procedure is included in the Experimental Section.

**Figure 2(a)** shows comparative FTIR spectra corresponding to GNSs, before functionalization (*i.e.*, with only lipoic acid on their surface), and after anti-ICAM-1 and anti-PS functionalization. Lipoic acid, as a ligand, displays a characteristic broad O-H stretch vibration peaking at around  $3425\text{ cm}^{-1}$ , a C=O stretch at  $1676\text{ cm}^{-1}$  and a C-O vibration at  $1085\text{ cm}^{-1}$ . (i) After functionalization with the peptide (anti-ICAM-1) the broad O-H band has increased relative to the other bands, due to the presence of more hydrogen bonding in the peptide. Additionally, the C=O double bond is slightly shifted to shorter wavenumber ( $1646\text{ cm}^{-1}$ ), which is typically observed when moving from the acid to the amide.<sup>[30]</sup> The C-O vibration is drastically reduced in intensity, revealing a relative decrease of C-O bonds, which also goes along with a shift from acid to amide. (ii) The functionalization of the GNS with PEG (used to link the nanoparticle to anti-PS) shows a broad band between  $497\text{-}717\text{ cm}^{-1}$  which is characteristic of the Au-S bond between the thiol group on the PEG and the GNS. It also shows an O-H stretch at  $3407\text{ cm}^{-1}$ . The addition of the anti-PS can be characterised by a broad band at  $620\text{-}880\text{ cm}^{-1}$  and a narrow peak at  $3371\text{ cm}^{-1}$  which is characteristic of the NH bond. The C=O stretch is common between the PEG functionalized GNS and the GNS functionalized with PEG and anti-PS.

Both the anti-ICAM-1 or anti-PS surface decorations should make the specific targeting of damaged cardiomyocytes possible, as illustrated in **Figure 1(c)**.

**Figure 2(b)** includes the Dynamic Light Scattering (DLS) spectra as obtained for GNSs before and after anti-PS and anti-ICAM-1 functionalization. The hydrodynamic radius of the original (non-functionalized) GNSs is 200 nm in very good agreement with the TEM data (**Figure 1(a)**). Anti-ICAM-1 and anti-PS functionalization increases this hydrodynamic radius up to about 300 and about 600 nm, respectively. Despite this substantial increment in the hydrodynamic size, the biofunctionalized GNSs kept their stable colloidal character, without evidence for



agglomeration over weeks. On the other hand, the uptake of these rather large GNSs by the reticuloendothelial system is a possible concern since it might reduce the circulating time of the GNSs, compromising the specific labelling. This aspect should be tested in future experiments. To verify the molecular specificity of the anti-PS GNSs, *in vitro* experiments regarding endothelial cells (HUVEC) cultures were carried out. We compared the dark field microscopy images of healthy and apoptotic (DMSO treated) cell cultures after being incubated with functionalized (anti-PS) and non-functionalized GNSs. The highest amount of GNSs (red spots) attached to endothelial cells is found in the apoptosis-induced culture incubated with anti-PS functionalized GNSs (see **Figure S2** in the Supporting Information section).

**Figure 3(a)** shows a schematic representation of the Langendorff model used in this work. Experimental details can be found in the Experimental Section. Briefly, the rat heart is mounted in the perfusion system and local ischemia is induced by a ligature of the left anterior descending coronary artery. The occlusion time was varied between 0 and 60 min. The ischemic area was detected by staining heart slices with tetrazolium (**Figure 3(b)**). After coronary occlusion, hearts were perfused either with a solution without GNSs (vehicle) or with a solution containing biofunctionalized GNSs.

As mentioned in the introduction section, PS translocates to the outer leaflet of the cell membrane of apoptotic cells. In order to test this phenomenon, we stained PS by perfusing ischemic hearts with fluorescent Annexin V (see a detailed description in the experimental section). As expected, our results show an increased Annexin V staining in the infarcted tissue compared to the healthy one (**Figure 3(c)**). Green areas in **Figure 3(c)** are due to the fluorescent Annexin V staining, while blue dots represent the cells nuclei due to DAPI staining.

Likewise, previous works postulated the overexpression of ICAM-1 in myocardial tissue after an ischemic event. In order to confirm such overexpression, we measured by Western Blot analysis the ICAM-1 protein content in control hearts and in hearts subjected to local ischemia-reperfusion (IR) for 15, 30, 45 or 60 min. A detailed description of the experimental procedure

can be found in the Experimental Section. Data included in **Figure 3(d)** reveal a slight, but significant, overexpression of ICAM-1 in ischemic hearts compared to the controls. The Western Blot images included in **Figure 3(d)** correspond to representative examples extracted from the complete assay that is provided in the Supporting Information (**Figure S3**). Furthermore, ICAM-1 overexpression was also assessed by immunofluorescence in slices of hearts subjected to 60 min of focal ischemia, showing increased ICAM-1 staining in ischemic tissue compared to non-ischemic tissue (**Figure 3(e)**). The slight overexpression of ICAM-1 detected by Western Blot may be explained by the short duration of the ischemic event, since it is reported that ICAM-1 levels increase slowly in the damaged tissue and remained elevated for several days.<sup>[22]</sup> This is at variance to the case of the AT1R protein, an excellent label of damaged cardiovascular tissues due to its high overexpression after acute myocardial infarction. Previous works have reported an almost linear increment of AT1R in infarcted hearts with the ischemia duration.<sup>[31]</sup> Although we did not find a clear evidence that longer ischemia events lead to larger overexpression of PS and ICAM-1 proteins, imaging experiments were all carried out by using hearts subjected to 60 min ischemia events.

For visualization of the damaged myocardium sites, the catheter of the intravascular OCT system was introduced into the left ventricle of the rats' heart after being subjected to the infarct, as is schematically represented in **Figure 4(a)**. Technical specifications of the OCT system used in this work are given in the Experimental Section. Under the used experimental arrangement, the cross-sectional images account for the OCT signal provided by both healthy and infarcted tissues. In presence of functionalized GNSs at the damaged myocardium tissues, the OCT intensity is expected to increase due to their enhanced backscattering cross section (**Figure 4(b)**).

**Figure 5 (a)** includes the cross-sectional OCT images of a control heart subjected to a 60 min ischemia. The control case corresponds to the infarcted heart but just perfused with vehicle (*i.e.*, with a solution without GNSs). The area affected by the ligation of the anterior descending

coronary artery is indicated as “infarcted”, whereas the myocardium tissue not irrigated by the occluded artery is indicated as “healthy”. In the control case, the OCT brightness obtained in the infarcted and healthy areas seem to be very similar. The comparable OCT signal obtained from healthy and damaged myocardium in absence of GNSs is further evidenced in **Figure 5(b)**, that shows in-depth OCT intensity averaged profiles obtained in both the healthy and infarcted tissues. We should mention here that these profiles correspond to an average over 10 individual radial intensity depth profiles. In order to quantify the total OCT intensity in both healthy and infarcted myocardium we define the integrated OCT signal as:

$$I_{OCT} = \int I_{OCT}(z)dz \quad (1)$$

where  $I_{OCT}(z)$  is the OCT intensity at depth  $z$  ( $z$  ranging from 0 up to 2 mm). In the control hearth (*i.e.*, without post-infarct GNSs perfusion), we have estimated that the integrated OCT signals at the healthy and infarcted tissues are  $I_{OCT}^c(health) = 0.80 \pm 0.07$  and  $I_{OCT}^c(Inf) = 0.76 \pm 0.04$ , respectively (**Figure 6(a)**). In  $I_{OCT}^c(Inf)$  and  $I_{OCT}^c(health)$ , the superscript  $c$  stands for control. The normalized OCT contrast ( $\Delta I_{OCT}^{norm}$ ) can be defined as:

$$\Delta I_{OCT}^{norm} = \frac{I_{OCT}(inf) - I_{OCT}(health)}{I_{OCT}(health)} \quad (2)$$

For the control heart (*i.e.*, without any contrast agent), we have obtained  $\Delta I_{OCT}^{norm,c} \approx -4,9\%$  (**Figure 6(b)**). Thus, the careful analysis of depth profiles reveals that the OCT intensity is slightly larger in the healthy tissues. In absence of any exogenous contrast agent, the OCT signal provided by a given tissue depends on its scattering and extinction properties. Therefore, experimental data suggest that the back-scattering coefficient of the myocardium decreases due to the ischemic event. This is, indeed, in agreement with previous results published by D. Abookasis *et al.* who found that the wavelength-dependence of the reduced scattering (*i.e.*, scatter power) of brain tissues decreases significantly after an ischemic event.<sup>[32]</sup> Not only that, our findings are also in good agreement with the results published by S. Akter and co-workers

who, using a single-reflectance fiber probe, found that the scattering coefficient of the liver decreased during an ischemic event.<sup>[33]</sup>

The small difference between the OCT integrated signal from healthy and infarcted tissues clearly indicates that detection of infarcted sites by OCT requires the use of contrast agents that would enhance the OCT signal difference between infarcted and healthy tissues.

As a second control, the accumulation of non-functionalized GNSs has been tested. For this purpose, a heart subjected to a lipoic acid-coated GNSs dispersion perfusion has been imaged. Lipoic acid does not provide a specific functionalization besides enhancing the aqueous colloidal stability of GNSs. **Figures 5(c) and 5(d)** show the cross-sectional image and in-depth averaged intensity profile of a heart after perfusion with lipoic-acid coated GNSs, respectively. Further analysis of these profiles verifies the slightly larger scattering of healthy tissue seen in the control heart (vehicle solution) as also manifested in **Figure 6(a)** (please remember that this larger scattering is due to the tissue scattering but not to the contrast). In particular,  $I_{OCT}^{LA}(inf) = 0.73 \pm 0.02$  and  $I_{OCT}^{LA}(health) = 0.80 \pm 0.01$  (LA stands for lipoic acid), which leads to a normalized OCT contrast of  $\Delta I_{OCT}^{norm,LA} \approx -9\%$  (**Figure 6(b)**), as defined in expression (2).

**Figure 5(e)** shows the cross-sectional image of an infarcted heart subjected to a perfusion with anti-PS functionalized GNSs. In this case, the infarcted tissue shows a larger OCT signal than the healthy one, indicating an enhanced backscattering signal of infrared light. This is further evidenced in **Figure 5(f)** that includes the OCT intensity profiles as obtained from both healthy and infarcted tissues (profiles have been obtained by averaging the OCT signal along 10 radial scans). We attribute the larger OCT signal to the presence of anti-PS functionalized GNSs and to their high scattering cross section at the OCT wavelength. In this case, the OCT signal accounts for the backscattering signal generated by tissues plus that generated by GNSs adhered to the damaged cardiomyocytes. Such adhesion reveals the cell damage (apoptosis) caused by the 60 min ischemic event. Analysis of the profiles given in **Figure 5(d)** leads to  $I_{OCT}^{PS}(inf) =$

$1 \pm 0.03$  and  $I_{OCT}^{PS}(health) = 0.89 \pm 0.04$ , where the superscript *PS* stands for the anti-PS functionalization (see **Figure 6(a)**). The normalized OCT contrast is  $\Delta I_{OCT}^{norm,PS} \approx +13\%$ . Note that the presence of the GNSs at the damaged tissues has turned the normalized OCT contrast from negative (for the vehicle and lipoic acid coated GNSs solutions) to positive (in the heart perfused with anti-PS GNSs).

Finally, **Figure 5(g)** corresponds to the OCT cross-sectional images of an infarcted heart after being subjected to a reperfusion with anti-ICAM-1 functionalized GNSs. **Figure 5(h)** shows the averaged in-depth profiles of the OCT intensity as obtained from both healthy and infarcted tissues. Again, the perfusion with functionalized GNSs provides a clear enhancement of the OCT signal generated at the infarcted myocardial tissues sites in respect to the healthy sites. As a matter of fact, the analysis of the experimental data included in **Figure 5(g)** leads to  $I_{OCT}^{IC}(inf) = 1.00 \pm 0.02$  and  $I_{OCT}^{IC}(health) = 0.82 \pm 0.01$ , where the superscript *IC* stands for the anti-ICAM-1 functionalization (see **Figure 6(a)**). The normalized OCT contrast, as defined in expression (2), is  $\Delta I_{OCT}^{norm,IC} \approx +22\%$  (**Figure 6(b)**).

Consequently, it seems that, in the infarcted myocardium, both the anti-ICAM-1 and anti-PS functionalization produce an enhancement in the OCT signal that is clearly detectable by OCT. Although further experiments, including *in vivo*, would be necessary to verify this conclusion, it seems that targeting inflammation could be as good as targeting apoptosis for infarcted myocardium imaging at the molecular level.

**Figure 6(a)** and **6(b)** demonstrate how intensity-based analysis of OCT images can be used for detection of ischemic tissues by using GNSs as contrast agents. However, the presence of GNSs in a given necrotic area should not only produce an intensity enhancement but also a reduction in the light penetration depth. In fact, GNSs do not only scatter but also absorb the OCT infrared laser radiation. Thus, the presence of GNSs in a tissue does not only increases its effective back scattering cross section but also its effective extinction coefficient ( $\alpha_{ext}^{eff}$ ) and so, reducing the

light penetration depth. In a first order approximation, the depth dependence of the OCT signal is given by:

$$I_{OCT}(z) = I_{OCT}(z = 0) \times \exp(-\alpha_{ext}^{eff} z) = I_{OCT}(z = 0) \times \exp\left(-\frac{z}{d_{eff}}\right) \quad (3)$$

where  $d_{eff} = 1/\alpha_{ext}^{eff}$  is the effective penetration length. Thus, the presence of GNSs should cause a reduction in  $d_{eff}$ . The penetration depths of OCT radiation in healthy and infarcted tissues in the four cases under study were calculated by fitting the  $I_{OCT}(z)$  experimental profile data to expression (3). In all the cases, the ischemic process leads to a decrease in  $d_{eff}$  when compared to the values of the healthy tissue, as expected. Therefore, the change in  $d_{eff}$  can be used as a complementary indicator of the infarcted myocardium. As for the normalized OCT contrast ( $\Delta I_{OCT}^{norm}$ ), we can now define the normalized change in the OCT penetration length:

$$\Delta d_{eff}^{norm} = \frac{d_{eff}(health) - d_{eff}(inf)}{d_{eff}(health)} \quad (4)$$

From data given in **Figure 6(c)** we have estimated for the control heart and the one perfused with lipoic acid-coated GNSs values of  $\Delta d_{eff}^{norm,C} \approx 9\%$  and  $\Delta d_{eff}^{norm,LA} \approx 14\%$ , and  $\Delta d_{eff}^{norm,IC} \approx 17\%$ ,  $\Delta d_{eff}^{norm,PS} \approx 26\%$  for inflammation and apoptosis molecular targeting with functionalized GNSs, respectively (**Figure 6d**). This enhancement also indicates the presence of GNSs in the infarcted tissues, this fact being in good agreement with the results obtained by intensity-analysis of OCT images.

Therefore, data included in **Figure 6** indicate that detection of infarcted myocardium using functionalized GNSs as contrast agents can be achieved either by intensity analysis or by the determination of the effective penetration length of OCT radiation.

Finally, it should be noted that efficient targeting of the infarcted tissues at the *in vivo* level would, in principle, benefit long circulation times that are not expected for our over 200 nm gold nanoparticles. In any case, we would recall that recent results have also demonstrated how

efficient *in vivo* imaging of infarcted heart is possible by using nanoparticles with low circulation times.<sup>[31b]</sup>

### 3. Conclusion.

In summary, the ability of biofunctionalized gold nanoshells for imaging of the infarcted myocardium has been explored. Two different strategies were followed: targeting inflammation and apoptosis, both taking place simultaneously in cardiomyocytes after an ischemic event. For that purpose, gold nanoshells have been properly functionalized to provide them with specific affinity to cardiomyocytes overexpressing either the intercellular adhesion molecule 1(ICAM-1) or the phosphatidylserine enzyme (PS). *Ex vivo* results in rat hearts demonstrate the ability of both functionalizations to induce selective accumulation of gold nanoshells at damaged myocardial tissues. Such selective accumulation causes an enhancement in the back-scattered light efficiency and, therefore, makes the infarcted tissue visible by infrared intravascular Optical Coherence Tomography (OCT). Visualization of infarcted myocardial tissues is possible by two different approaches: either by the analysis of the total OCT signal or by the determination of the penetration length of OCT radiation into tissues.

These results pioneers the first demonstration of molecular imaging of infarcted hearts by combining an operational clinical technique (intravascular OCT) with optical nanoprobe currently undergoing clinical testing, such as gold nanoshells. This work constitutes the first step towards fast and accurate diagnosis of infarcted hearts at molecular level, by using non-ionizing (safe) radiation and biocompatible gold nanoparticles. Once the potential of functionalized plasmonic nanoparticles for molecular imaging of infarcted myocardium is demonstrated, their translation to the *in vivo* and to the clinics requires a comprehensive study on the toxicity and stability of these > 200 nm nanoparticles.

#### 4. Experimental section

*Anti-PS functionalization of gold nanoshells.* For the anti-PS biofunctionalization, we employed GNSs dispersions in PBS at an initial concentration of  $0.05 \text{ mg mL}^{-1}$  ( $8.5 \times 10^8$  particles  $\text{mL}^{-1}$ ), carboxyl thiolated PEG (CT-PEG 12) from Thermo Scientific with a MW 634.77 and stock concentration 0.105 M, and PEG dissolved using 1.5 mL MilliQ-grade water (from now on just water). The 1-Ethyl-3-(3'-dimethylaminopropyl)carbodiimide (EDAC) buffer was prepared using 2% w/v EDC and 3% w/v NHS in PBS and anti-phosphatidylserine from Merck Millipore ( $1 \text{ mg mL}^{-1}$ ) was used. We first proceeded with the PEGylation of gold nanoshells according to the following steps: i) 1.5 ml CT-PEG diluted in water (with a final concentration of 0.01 M) was added in a 1:1 ratio to a glass vial containing 5 mL of a GNS/PBS dispersion ( $0.05 \text{ mg mL}^{-1}$ ) under sonication. This mixture was sonicated for 5 minutes, and then magnetically stirred for 1 hour at room temperature with a speed of about 760 rpm. ii) The PEGylated GNSs were transferred to an eppendorf tube and centrifuged at 5600 rpm for 10 minutes. Then the supernatant was discarded, the pellet washed with water and redispersed under sonication. The wash cycle was performed 3 times to remove the excess of PEG. iii) The final pellet was re-dispersed using 5 mL of Hank's balanced salt solution (HBSS). Then 1 mL aliquot was removed for characterisation by Fourier-transform spectroscopy (FTIR) and Dynamic Light Scattering (DLS).

After PEGylation we proceeded with the conjugation of anti-phosphatidylserine antibody (aPS) to the PEG-Gold Nanoshells using EDC according to the following steps: i) In a glass vial under a sterile fume hood, 4 mL of the GNS-PEG was mixed with 400  $\mu\text{L}$  EDAC buffer. 40  $\mu\text{L}$  of anti-PS solution was slowly added to this mix (1:0.1:0.01 ratio). ii) The dispersion was magnetically stirred at room temperature for 2 hours at a speed close to 760 rpm. iii) After 2 hours, the reaction was quenched with 80  $\mu\text{L}$  1 M hydroxylamine for 10 minutes. iv) The solution was transferred to 1 mL eppendorf tubes and centrifuged for 10 minutes at 5600 rpm. The supernatant was discarded, the pellet washed with PBS and re-dispersed under sonication.



The washing cycle was repeated 3 times. The final pellet was re-dispersed in a total of 5 mL PBS and stored at 4 °C. v) While scaling up the production of GNS-PEG-anti-PS, the same ratios of reagents as mentioned above were used.

*Anti-ICAM-1 functionalization of gold nanoshells.* The commercial dispersion of GNSs coated with lipoic acid (10 mL, 0.5 mg) in PBS was centrifuged (4000 rcf, 30 min) and washed 2x with DMSO (1.5 mL) and then carefully dispersed in DMSO (1.5 mL). *N*-hydroxysuccinimide (NHS; 5.66 mg, 49.18  $\mu$ mol), followed by 1-Ethyl-3-(3-dimethylaminopropyl) carbodiimide (EDC; 5.98 mg, 38.55  $\mu$ mol) were added to the mixture and then careful sonication and stirring were alternated for 30 min. Afterwards, the dispersion was centrifuged (4000 , 20 min), washed 2x with DMSO (1.5 mL), and then the supernatant solvent was removed and the activated GNSs were dispersed in borate buffer (1.5 mL, pH 8) and sonicated. The cLABL peptide (cyclo(1,12)PenITDGEATDSGC 0.33 mg, 0.28  $\mu$ mol) was added and, after sonication for 30 min, the mixture was stirred overnight before being quenched with a few drops of 1 M glycine and stirred for another 30 min. Finally, the mixture was centrifuged (4000 rcf, 30 min), washed twice with PBS (2 mL and 1.5 mL) and then carefully re-dispersed in PBS (10 mL).

*Langendorff model of an infarcted heart.* Male Sprague-Dawley rats (300 g body weight) were fed *ad libitum* with a standard chow and housed in quarters with a 12 h light cycle and under controlled conditions of humidity (50-60%) and temperature (22-24 °C). All the experiments were conducted according to the European Union Legislation (Directive 2010/63/UE) and with the approval of the Animal Care and Use Committee of the Autonomous University of Madrid (approval number CEI-83-1537). The hearts were removed from rats anesthetized with intraperitoneal injection of sodium pentobarbital (100 mg/kg) followed by an intravenous injection of heparin (1,000 IU). Hearts were cannulated through the aorta and subjected to retrograde perfusion (11-15 mL/min, 70 mmHg) with Krebs-Henseleit buffer (95% oxygen and 5% carbon dioxide) (pH 7.3). Coronary perfusion and left ventricular pressures were measured through a transducer laterally connected to the perfusion cannula and through a latex balloon

inserted in the left ventricle, respectively. After 30 min of equilibration, partial ischemia was induced by ligation of the left anterior descending coronary artery. The artery was kept occluded for 15, 30, 45 or 60 min. After ischemia, the ligation was released, and the heart was subjected to 30 min of reperfusion. Finally, the perfusion system was modified to a closed circuit, in which a dispersion containing 1 mL of a colloidal dispersion of GNSs in PBS ( $0.035 \text{ mg mL}^{-1}$ ) was kept circulating with a residual volume of 9 mL for another 30 minutes. A control heart was also studied for the purpose of comparison. In this case, the perfusion was performed with a vehicle solution (i.e. without GNSs). Importantly, all animals used in this study were male as the estrous phase in female rats might affect the severity of ischemia-reperfusion. Indeed, it is reported that female gender favourably influences the remodelling and the adaptive response of the heart to myocardial infarction.

*Tetrazolium staining.* After 60 min of ischemia and 45 of reperfusion in the Langendorff system, hearts were frozen for 1h at  $-20^\circ\text{C}$ . Afterwards, hearts were transversely cut into 1 mm slices and incubated with tetrazolium (T-8877, Sigma-Aldrich, St. Louis, MO, USA) 1% in PBS for 25 min at  $37^\circ\text{C}$ . The slices were then fixed in 4% paraformaldehyde (PFA) overnight at  $4^\circ\text{C}$ . Images were acquired using a Stereo Microscope (SMZ645, Nikon, Tokyo, Japan).

*Determination of ICAM-1 protein content in infarcted hearts.* 100 mg of cardiac tissue were homogenized using RIPA buffer. After centrifugation (12.000 rpm,  $4^\circ\text{C}$ , 20 min), the supernatant was collected and the total protein content was determined by the Bradford assay (Sigma-Aldrich, St. Louis, MO, USA). For each protein determination, 100  $\mu\text{g}$  of total protein were loaded in each well and subjected to electrophoresis using resolving acrylamide (8-12%) SDS gels (Bio-Rad, Héracles, CA, USA). Afterwards, proteins were transferred to polyvinyl difluoride (PVDF) membranes (Bio-Rad, Héracles, CA, USA). Transfer efficiency was determined by Ponceau red dyeing (Sigma-Aldrich, St. Louis, MO, USA). Membranes were then blocked either with Tris-buffered saline (TBS) containing 5% (w/v) non-fat dried milk and incubated with the primary antibody against ICAM-1 (Abcam #ab-33894; 1:1000). Membranes

were subsequently washed and incubated with the secondary antibody conjugated with peroxidase (1:2000; Pierce, Rockford, IL, USA). Peroxidase activity was visualized by chemiluminescence and quantified by densitometry using BioRad Molecular Imager ChemiDoc XRS System (Hércules, CA, USA). Finally, in order to normalize each sample for gel-loading variability, membranes were incubated with a primary antibody against the constitutive protein GAPDH (1:1000; Ambion Life Technologies, Waltham, MA, USA). For each sample, the relative protein expression levels were calculated in relation to protein expression levels in non-ischemic hearts. As shown in **Figure S3** of the Supporting Information section, all samples were run in the same assay.

*Determination of PS by staining with fluorescent Annexin V.* After 60 min of ischemia in the Langendorff system, hearts were perfused in a close circuit with Annexin V-iFluor 488 (ab219904, ABCAM, Cambridge, UK) diluted 1:2 in Annexin V buffer (10 mM HEPES, 140 mM NaCl, 2,5 mM CaCl<sub>2</sub>, pH 7,4) and 1:50 in 10 ml of Krebs buffer. After 45 min of perfusion with annexin V, hearts were collected and fixed in 4% paraformaldehyde (PFA) overnight. Afterwards the tissue was dehydrated, embedded in paraffin wax and cut in 5 µm sections using a microtome. Sections were then displayed in superfrost slides, deparanized with xylol, rehydrated and washed with distilled water. Finally, sections were incubated with DAPI (4',6-Diamidino-2-phenylindole) 1/1000 for 5 minutes and mounted using ProLong Gold (Thermo Fisher Scientific, Hampton, NA, USA).

Images were acquired using a Nikon Eclipse Ti2-U microscope with 40x 0,65 NA objective (Nikon, Japan).

*Determination of ICAM-1 by immunofluorescence.* After 60 min of ischemia and 45 of reperfusion in the Langendorff system, hearts were fixed overnight in 4% paraformaldehyde (PFA). Afterwards they were dehydrated, embedded in paraffin wax, and cut on 5 µm sections using a microtome. Sections were then displayed in superfrost slides, deparanized with xylol, rehydrated and washed in distilled water. Slices were then heated in citrate uffer pH 6 for

antigen retrieval. Several washings were performed before blocking for 30 min with 5% BSA in PBS and incubating with the primary antibody for ICAM-1 (ab206398, ABCAM, Cambridge, UK) 1:100 at 4 °C overnight. Slides were then washed and incubated for 1 h with the fluorescent secondary antibody F488 (111-547-003, Jackson ImmunoResearch Europe Ltd, Cambridge, UK) diluted 1:300 in PBS. Nuclei were counterstained with DAPI 1/1000 for 5 min and. Finally, slices were mounted with ProLong Gold (Thermo Fisher Scientific, Hampton, NA, USA).

Images were acquired using a Leica SP5 confocal microscope fitted with a 40x 1.25 NA objective (Wetzlar, Germany). Z-stacks were taken every 2 µm. Maximal projections of images were 3D reconstructed in whole-mount views using FIJI for Windows 36bit (NIH, Bethesda, MA, USA).

*Optical Coherence Tomography.* The OCT system used all along this work is a commercially available cardiovascular OCT (CV-OCT) imaging system model Dragon-Fly™ (St. Jude Medical, St. Paul, MN, USA). Details about this system can be found elsewhere.<sup>[34]</sup> The CV-OCT system incorporates a compact super-luminescent diode operating at a central wavelength of 1320 nm with a bandwidth of 200 nm. The infrared radiation is coupled to a single mode fiber incorporated inside a 0.9 mm diameter catheter. The output end of the fiber is connected to a rotating reflector that deviates and scans the 1320 nm radiation in an orthogonal plane in respect to the fiber. The reflector also collects the back-scattered signal and couples it into the single mode fibre. The single-mode fiber is optically connected to an interferometer working in the frequency domain, so that it can reconstruct cross sectional images at the position of the reflector. The axial resolution of our CV-OCT system was approximately 15 µm, with a penetration length larger than 3 mm.

### **Supporting Information**

Supporting Information is available from the Wiley Online Library or from the author.

**Acknowledgements**

This work was partially supported by the Ministerio de Economía y Competitividad de España (MAT2016-75362-C3-1-R) and (MAT2017-83111R), by the Instituto de Salud Carlos III (PI16/00812) and (PI19/00565), by the Comunidad Autónoma de Madrid (B2017/BMD-3867RENIMCM), and co-financed by the European Structural and investment fund. Additionally, the research was financed by the European Commission Horizon 2020 project NanoTBTech, the Fundación para la Investigación Biomédica del Hospital Universitario Ramón y Cajal project IMP18\_38 (2018/0265), and also by COST action CA1740. D. H. O. is grateful to the Instituto de Salud Carlos III for a Sara Borrell scholarship (CD17/00210).

The authors want to acknowledge Prof. Luis Santamaría Solís and Carmen Sánchez Palomo from the Department of Histology (School of Medicine, UAM) for their invaluable help with the histological studies.

Received: ((will be filled in by the editorial staff))

Revised: ((will be filled in by the editorial staff))

Published online: ((will be filled in by the editorial staff))

## References

- [1] a) M. Yu, M. T. Guaraldi, M. Mistry, M. Kagan, J. L. McDonald, K. Drew, H. Radeke, M. Azure, A. Purohit, D. S. Casebier, S. P. Robinson, *Journal of Nuclear Cardiology* **2007**, 14, 789; b) V. M. Ferreira, S. K. Piechnik, M. D. Robson, S. Neubauer, T. D. Karamitsos, *Journal of Thoracic Imaging* **2014**, 29, 147; c) L. J. Anderson, S. Holden, B. Davis, E. Prescott, C. C. Charrier, N. H. Bunce, D. N. Firmin, B. Wonke, J. Porter, J. M. Walker, D. J. Pennell, *European Heart Journal* **2001**, 22, 2171; d) R. S. Driessen, P. G. Raijmakers, W. J. Stuijzand, P. Knaapen, *The International Journal of Cardiovascular Imaging* **2017**, 33, 1021; e) C. Rischpler, S. G. Nekolla, I. Dregely, M. Schwaiger, *Journal of nuclear medicine : official publication, Society of Nuclear Medicine* **2013**, 54, 402; f) P. Rivera Gil, D. Hühn, L. L. del Mercato, D. Sasse, W. J. Parak, *Pharmacological Research* **2010**, 62, 115.
- [2] J. Qiu, R. Zhang, J. Li, Y. Sang, W. Tang, P. Rivera Gil, H. Liu, *Int J Nanomedicine* **2015**, 10, 6709.
- [3] J. C. Stendahl, A. J. Sinusas, *Journal of nuclear medicine : official publication, Society of Nuclear Medicine* **2015**, 56, 1469.
- [4] J. Hu, D. H. Ortgies, E. Martín Rodríguez, F. Rivero, R. Aguilar Torres, F. Alfonso, N. Fernández, G. Carreño-Tarragona, L. Monge, F. Sanz-Rodriguez, M. d. C. Iglesias, M. Granado, A. L. García-Villalon, J. García Solé, D. Jaque, *Advanced Optical Materials* **2018**, 6, 1800626.
- [5] a) W. Jiang, M. Almadi, N. Salas, S. Rajguru, *Optical properties of biological tissues measured at infrared wavelengths*, **2014**; b) E. Hemmer, A. Benayas, F. Légaré, F. Vetrone, *Nanoscale Horizons* **2016**, 1, 168.
- [6] C. Louis, O. Pluchery, *Gold Nanoparticles for Physics, Chemistry and Biology*.
- [7] a) M. Grzelczak, J. Pérez-Juste, P. Mulvaney, L. M. Liz-Marzán, *Chemical Society Reviews* **2008**, 37, 1783; b) G. Wang, Y. Lu, C. Yan, Y. Lu, *Sensors and Actuators B: Chemical* **2015**, 211, 1; c) S. Zeng, K.-T. Yong, I. Roy, X.-Q. Dinh, X. Yu, F. Luan, *Plasmonics* **2011**, 6, 491; d) J. Zhou, J. Ralston, R. Sedev, D. A. Beattie, *Journal of Colloid and Interface Science* **2009**, 331, 251; e) Y. C. Wang, E. Rheume, F. Lesage, A. Kakkar, *Molecules (Basel, Switzerland)* **2018**, 23.
- [8] a) S. Hirn, M. Semmler-Behnke, C. Schleh, A. Wenk, J. Lipka, M. Schäffler, S. Takenaka, W. Möller, G. Schmid, U. Simon, W. G. Kreyling, *Eur. J. Pharm. Biopharm.* **2011**, 77, 407; b) X.-D. Zhang, D. Wu, X. Shen, P.-X. Liu, N. Yang, B. Zhao, H. Zhang, Y.-M. Sun, L.-A. Zhang, F.-Y. Fan, *Int J Nanomedicine* **2011**, 6, 2071; c) C. Lopez-Chaves, J. Soto-Alvaredo, M. Montes-Bayon, J. Bettmer, J. Llopis, C. Sanchez-Gonzalez, *Nanomedicine* **2018**, 14, 1; d) W. D. James, L. R. Hirsch, J. L. West, P. D. O'Neal, J. D. Payne, *J. Radioanal. Nucl. Chem.* **2007**, 271, 455; e) M. Pannerec-Varna, P. Ratajczak, G. Bousquet, I. Ferreira, C. Leboeuf, R. Boisdard, G. Gapihan, J. Verine, B. Palpant, E. Bossy, E. Doris, J. Poupon, E. Fort, A. Janin, *Gold Bulletin* **2013**, 46, 257.
- [9] J. Hu, *Doctoral Thesis*, Universidad Autónoma de Madrid, Madrid, Spain, June, **2018**.
- [10] a) A. F. Versiani, L. M. Andrade, E. M. Martins, S. Scalzo, J. M. Geraldo, C. R. Chaves, D. C. Ferreira, M. Ladeira, S. Guatimosim, L. O. Ladeira, F. G. d. Fonseca, *Future Virology* **2016**, 11, 293; b) I. H. El-Sayed, X. Huang, M. A. El-Sayed, *Nano Letters* **2005**, 5, 829.
- [11] a) M. Varna, H. V. Xuan, E. Fort, *WIREs Nanomedicine and Nanobiotechnology* **2018**, 10, e1470; b) M. Y. Spivak, R. V. Bubnov, I. M. Yemets, L. M. Lazarenko, N. O. Tymoshok, Z. R. Ulberg, *EPMA Journal* **2013**, 4, 20; c) W. Lu, Q. Huang, G. Ku, X. Wen, M. Zhou, D. Guzatov, P. Brecht, R. Su, A. Oraevsky, L. V. Wang, C. Li, *Biomaterials* **2010**, 31, 2617; d) M. Wu, Y. Zhang, Y. Zhang, M. Wu, M. Wu, H. Wu,

- L. Cao, L. Li, X. Li, X. Zhang, *RSC Advances* **2018**, 8, 1706; e) R. Ravichandran, R. Sridhar, J. R. Venugopal, S. Sundarrajan, S. Mukherjee, S. Ramakrishna, *Macromolecular Bioscience* **2014**, 14, 515; f) V. P. Nguyen, Y. Li, W. Qian, B. Liu, C. Tian, W. Zhang, Z. Huang, A. Ponduri, M. Tarnowski, X. Wang, Y. M. Paulus, *Scientific Reports* **2019**, 9, 5945.
- [12] P. H. Kee, D. Danila, *Nanomedicine: Nanotechnology, Biology and Medicine* **2018**, 14, 1941.
- [13] a) D. Huang, E. Swanson, C. Lin, J. Schuman, W. Stinson, W. Chang, M. Hee, T. Flotte, K. Gregory, C. Puliafito, a. et, *Science* **1991**, 254, 1178; b) A. G. Podoleanu, J. A. Rogers, D. A. Jackson, *IEEE Journal of Selected Topics in Quantum Electronics* **1999**, 5, 1176; c) A. G. Podoleanu, M. Seeger, G. Dobre, D. Webb, D. Jackson, *Journal of Biomedical Optics* **1998**, 3.
- [14] a) J. Walther, M. Gaertner, P. Cimalla, A. Burkhardt, L. Kirsten, S. Meissner, E. Koch, *Anal. Bioanal. Chem.* **2011**, 400, 2721; b) G. F. James, presented at Proc.SPIE **1999**; c) I.-K. Jang, *Cardiovascular OCT imaging*, Springer, **2014**; d) F. Prati, E. Regar, G. S. Mintz, E. Arbustini, C. Di Mario, I.-K. Jang, T. Akasaka, M. Costa, G. Guagliumi, E. Grube, Y. Ozaki, F. Pinto, P. W. J. Serruys, f. t. E. s. O. R. Document, *European Heart Journal* **2009**, 31, 401.
- [15] T. Wang, J. J. Mancuso, S. M. S. Kazmi, J. Dwelle, V. Sapozhnikova, B. Willsey, L. L. Ma, J. Qiu, X. Li, A. K. Dunn, K. P. Johnston, M. D. Feldman, T. E. Milner, *Lasers in Surgery and Medicine* **2012**, 44, 49.
- [16] a) L. M. Maestro, P. Haro-González, A. Sánchez-Iglesias, L. M. Liz-Marzán, J. García Solé, D. Jaque, *Langmuir* **2014**, 30, 1650; b) J. Hu, F. Rivero, R. A. Torres, H. Loro Ramírez, E. M. Rodríguez, F. Alfonso, J. García Solé, D. Jaque, *Journal of Biophotonics* **2017**, 10, 674.
- [17] M. Mahmoudi, J. Meng, X. Xue, X. J. Liang, M. Rahman, C. Pfeiffer, R. Hartmann, P. R. Gil, B. Pelaz, W. J. Parak, P. del Pino, S. Carregal-Romero, A. G. Kanaras, S. Tamil Selvan, *Biotechnol. Adv.* **2014**, 32, 679.
- [18] Y. Geng, P. Dalhaimer, S. Cai, R. Tsai, M. Tewari, T. Minko, D. E. Discher, *Nature Nanotechnology* **2007**, 2, 249.
- [19] a) C. Zhou, T.-H. Tsai, D. C. Adler, H.-C. Lee, D. W. Cohen, A. Mondelblatt, Y. Wang, J. L. Connolly, J. G. Fujimoto, *Opt. Lett.* **2010**, 35, 700; b) E. Zagaynova, M. Shirmanova, A. Orlova, I. Balalaeva, M. Y. Kirillin, V. Kamensky, M. Bugrova, M. Sirotkina, *Gold nanoshells for OCT imaging contrast: From model to in-vivo study*, SPIE, **2008**.
- [20] a) A. M. Gobin, J. J. Moon, J. L. West, *Int J Nanomedicine* **2008**, 3, 351; b) A. R. Rastinehad, H. Anastos, E. Wajswol, J. S. Winoker, J. P. Sfakianos, S. K. Doppalapudi, M. R. Carrick, C. J. Knauer, B. Taouli, S. C. Lewis, A. K. Tewari, J. A. Schwartz, S. E. Canfield, A. K. George, J. L. West, N. J. Halas, *Proceedings of the National Academy of Sciences* **2019**, 116, 18590.
- [21] A. Lum, C. Green, G. Lee, D. Staunton, S. Simon, *The Journal of biological chemistry* **2002**, 277, 20660.
- [22] H. W. M. Niessen, P. A. J. Krijnen, C. A. Visser, C. J. L. M. Meijer, C. E. Hack, *Annals of the New York Academy of Sciences* **2002**, 973, 573.
- [23] a) K. Youker, C. W. Smith, D. C. Anderson, D. Miller, L. H. Michael, R. D. Rossen, M. L. Entman, *J Clin Invest* **1992**, 89, 602; b) K. Ban, U. Ikeda, M. Takahashi, T. Kanbe, T. Kasahara, K. Shimada, *Cardiovascular Research* **1994**, 28, 1258; c) R. Kacimi, J. S. Karliner, F. Koudssi, C. S. Long, *Circ Res* **1998**, 82, 576.
- [24] H. W. M. Niessen, W. K. Lagrand, C. A. Visser, C. J. L. M. Meijer, C. E. Hack, *Cardiovascular Research* **1999**, 41, 603.



- [25] G. L. Kukiela, C. W. Smith, A. M. Manning, K. A. Youker, L. H. Michael, M. L. Entman, *Circulation* **1995**, 92, 1866.
- [26] U. Ikeda, M. Ikeda, S. Kano, K. Shimada, *J Cardiovasc Pharmacol* **1994**, 23, 647.
- [27] N. Maulik, V. E. Kagan, V. A. Tyurin, D. K. Das, *American Journal of Physiology-Heart and Circulatory Physiology* **1998**, 274, H242.
- [28] D. Geldwerth, F. A. Kuypers, P. Bütikofer, M. Allary, B. H. Lubin, P. F. Devaux, *J Clin Invest* **1993**, 92, 308.
- [29] V. A. Fadok, D. R. Voelker, P. A. Campbell, J. J. Cohen, D. L. Bratton, P. M. Henson, *Journal of immunology (Baltimore, Md. : 1950)* **1992**, 148, 2207.
- [30] M. Hesse, H. Meier, B. Zeeh, **2002**, 1991.
- [31] a) D. H. Ortgies, Á. L. García-Villalón, M. Granado, S. Amor, E. M. Rodríguez, H. D. A. Santos, J. Yao, J. Rubio-Retama, D. Jaque, *Nano Research* **2019**, 12, 749; b) S. Mateos, J. Lifante, C. Li, E. C. Ximendes, T. Muñoz-Ortiz, J. Yao, M. de la Fuente-Fernández, Á. L. García Villalón, M. Granado, I. Zabala Gutierrez, J. Rubio-Retama, D. Jaque, D. H. Ortgies, N. Fernández, **2020**, 16, 1907171.
- [32] D. Abookasis, C. Lay, M. Mathews, M. Linskey, R. Frostig, B. Tromberg, *Journal of Biomedical Optics* **2009**, 14, 024033.
- [33] S. Akter, S. Maejima, S. Kawauchi, S. Sato, A. Hinoki, S. Aosasa, J. Yamamoto, I. Nishidate, *Journal of Biomedical Optics* **2015**, 20, 076010.
- [34] J. Hu, F. Sanz-Rodríguez, F. Rivero, E. M. Rodríguez, R. A. Torres, D. H. Ortgies, J. G. Solé, F. Alfonso, D. Jaque, *Nano Research* **2018**, 11, 676.



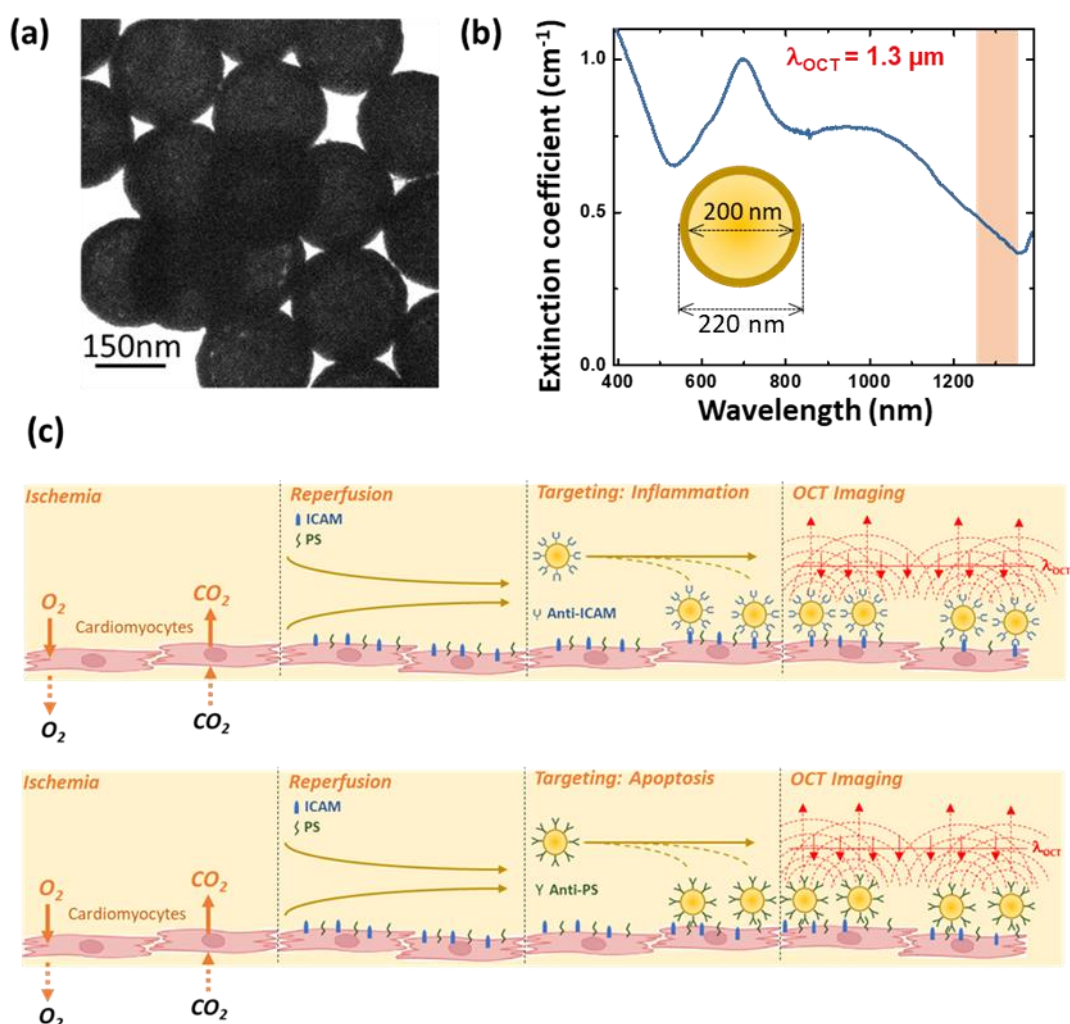


**Figure 1.** (a) TEM image of the gold nanoshells used all along this work. (b) Extinction spectrum of the GNSs used in this work. The operating wavelength of the intravascular OCT system used in this work is also indicated. (c) Schematic representation of the use of functionalized GNSs for molecular imaging of damaged cardiomyocytes in an ischemic event by Optical Coherence Tomography (OCT).

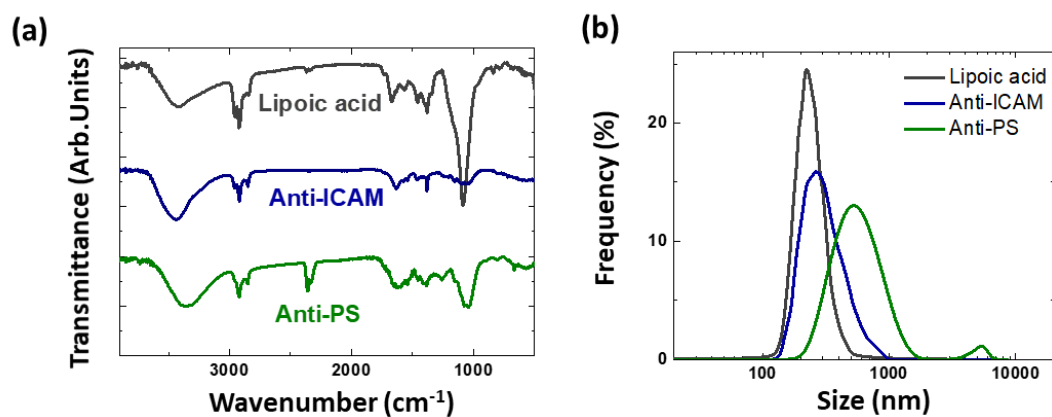


**Figure 2.** (a) Fourier Transform Infrared (FTIR) spectra corresponding to the three types of gold nanoshells used all along this work revealing their different surface decoration. (b) DLS spectra as obtained for the GNSs before (lipoic acid-coated) and after anti-PS and anti-ICAM-1 functionalization.

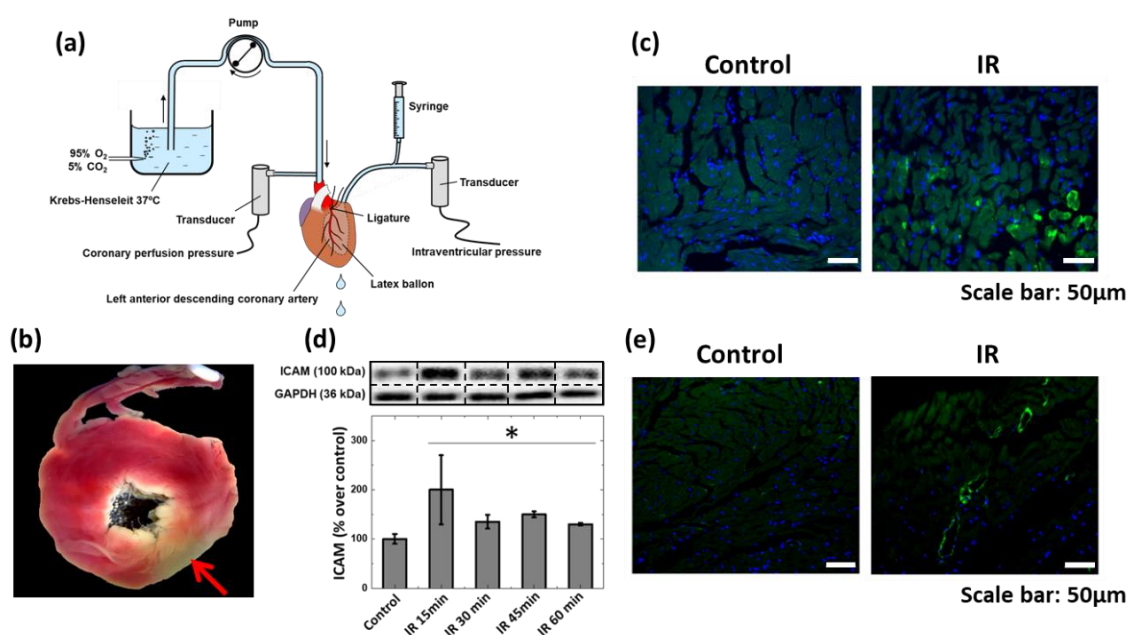


**Figure 3.-** (a) Schematic diagram of the experimental set-up used for the *ex-vivo* induction of an acute myocardial infarct in the heart of Sprague-Dawley rats using the Langendorff technique. (b) Representative image of a heart slice dyed with tetrazolium staining after being subjected to focal ischemia for 60 min and 45 min of reperfusion. (c) Detection of PS through binding to fluorescent Annexin V in healthy (control) and ischemic (IR) tissue. (d) Protein content of ICAM-1 in myocardial tissue from hearts subjected to increasing durations of coronary ischemia (15, 30, 45, and 60 min). Representative examples have been extracted from the complete assay (see **Figure S3**). Values are represented by the mean ± SEM. (n = 5 hearts/group). (e) Detection of ICAM-1 by immunofluorescence in healthy and ischemic tissue after 60 min of focal ischemia and 45 min of reperfusion.

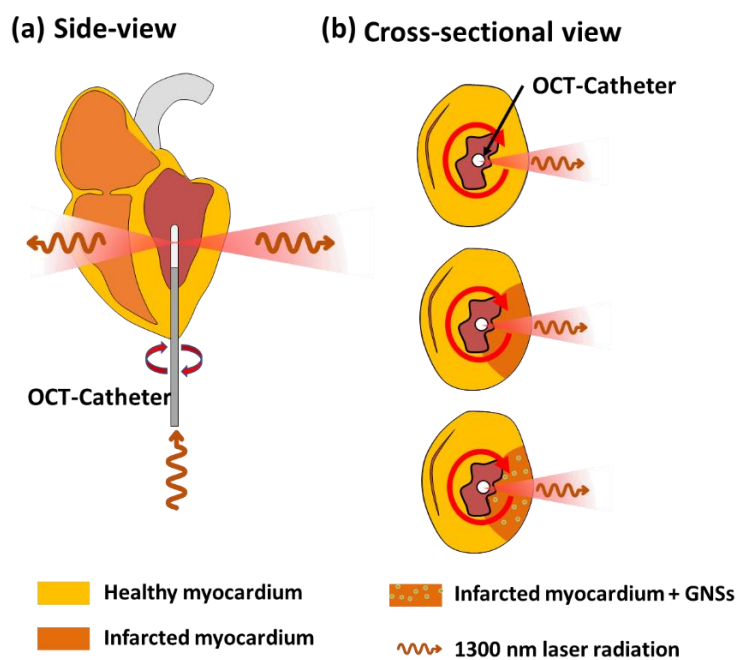


**Figure 4.** Side ((a)) and cross-sectional ((b)) drawing of an infarcted heart in the presence of the OCT rotating catheter for molecular visualization of damaged myocardium. In the cross-sectional views the cases of healthy or infarcted hearts after perfusion with vehicle (i.e., with a solution without functionalized GNSs) or with a solution of gold nanoshells are represented.

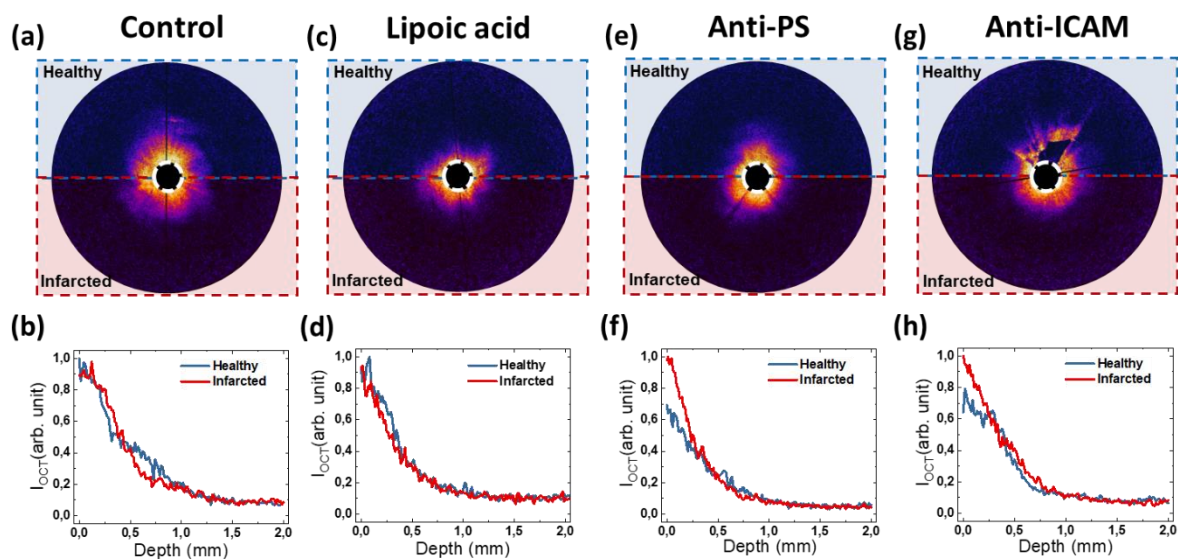


**Figure 5.** Comparative cross-sectional OCT images of healthy and infarcted tissues after reperfusion with; (a) vehicle (Control); (c) lipoic acid-coated (non-functionalized) (e) anti-PS functionalized GNSs and (g) anti-ICAM-1 (peptide) functionalized GNSs. (b), (d), (f) and (h) show the depth profiles of the averaged OCT signal calculated from the analysis of the OCT signal over ten radial scans.

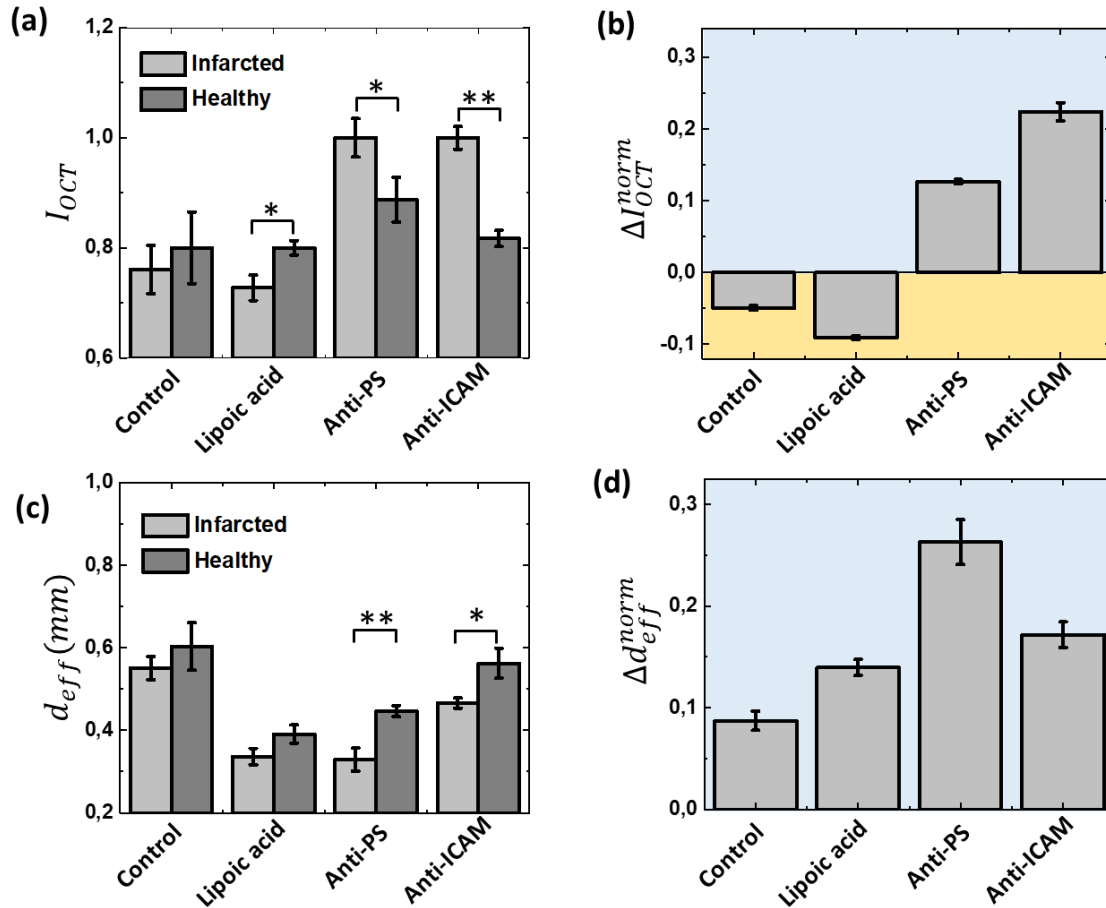


**Figure 6.** (a) Integrated OCT signal corresponding to healthy and infarcted myocardial tissues obtained from hearts submitted to an acute myocardial infarction (Infarcted) and perfused with a vehicle (control) and with a solution containing lipoic acid, anti-PS or anti-ICAM-1 coated gold nanoshells during reperfusion. (b) Normalized OCT contrast between infarcted and healthy tissues as obtained from hearts submitted to an acute myocardial infarction (Infarcted) and perfused with a vehicle (control) and with a dispersion of lipoic acid, anti-PS or anti-ICAM-1 coated gold nanoshells during reperfusion. (c) Calculated effective penetration length of the OCT signal for the control case, and hearts perfused with lipoic acid, anti-PS GNSs and anti-ICAM-1 coated GNSs (d) representation of the data in (c) after normalization. Significant statistical differences are given as determined by the paired sample t-test (\*p ≤ 0.05, \*\*p ≤ 0.01)

**Gold nanoshells emerge as new contrast agents for imaging of the infarcted myocardium by using Optical Coherence Tomography.** Suitable functionalization provides gold nanoshells with selective targeting capacities to both inflammation and apoptosis in cardiomyocytes and induces their accumulation at ischemia-induced damaged tissues. Localization of the infarcted myocardium is possible from the intensity- or penetration- based analysis of Optical Coherence Tomography images.

